Using Temperature-Sensitive Smart Polymers to Regulate DNA-Mediated Nanoassembly and Encoded Nanocarrier Drug Release

Kristen L. Hamner,[†,§] Colleen M. Alexander,[†,§] Kaitlin Coopersmith,[†] David Reishofer,[†] Christina Provenza,[‡] and Mathew M. Maye[†,‡,*]

[†]Department of Chemistry and [‡]Syracuse Biomaterials Institute, Syracuse University, Syracuse, New York 13244, United States. [§]K. L. Hamner and C. M. Alexander contributed equally to this work.

ABSTRACT In this paper we describe the use of a temperature-responsive polymer to regulate DNA interactions in both a DNA-mediated assembly system and a DNA-encoded drug delivery system. A thermoresponsive pNIPAAm-*co*-pAAm polymer, with a transition temperature (T_C) of 51 °C, was synthesized with thiol modification and grafted onto gold nanoparticles (Au NPs) also containing single-stranded oligonucleotides (ssDNA). The thermoresponsive behavior of the polymer regulated the accessibility of the sequence-specific hybridization between complementary DNA-functionalized Au NPs. At $T < T_C$, the polymer was hydrophilic and extended, blocking interaction between the complementary sequences at the periphery of the hydrodynamic diameter. In contrast, at $T > T_C$, the polymer shell undergoes a hydrophilic to -phobic phase transition and collapses, shrinking below the outer ssDNA, allowing for the sequence-specific hybridization to occur. The potential application of this dynamic interface for drug delivery is shown, in which the chemotherapy drug doxorubicin (DOX) is bound to double-stranded DNA (dsDNA)-functionalized Au NPs whose sequences are known to be high-affinity intercalation points for it. The presence of the polymer capping is shown to decrease drug release kinetics and equilibrium at $T < T_C$, but increase release at $T > T_C$, thus improving the cytotoxicity of the encoded nanocarrier design.

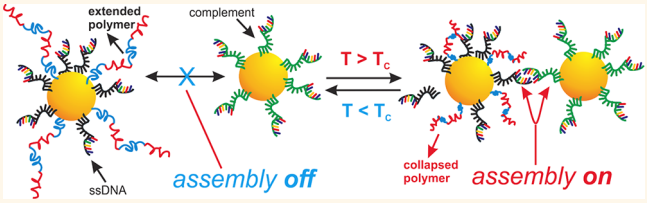

KEYWORDS: DNA · self-assembly · dynamic · responsive · nanoparticle · copolymer · smart

Today's chemists, physicists, engineers, and other technologists have an assortment of approaches to self-assemble nanomaterials from the bottom up.[1−4] These range from tailoring surface chemistry *via* self-assembled monolayer exchange[4−8] to addition of organic cross-linkers[9,10] or polymers and dendrimers[11−14] and by the introduction of biomolecular interactions. One biomolecular interaction in particular has proven to be both versatile and functional: that of using sequence-specific programming of DNA-mediated interactions between nanoparticles (NPs).[15−24] Using this approach, interaction energies between NPs can be tuned by manipulating DNA length and sequence, and important self-assembly parameters such as kinetics, denaturation temperatures, and interparticle distances can be tuned by changes to ionic strength, grafting density, and linker length.[15−19,24−29] For example, it was recently shown that the cooperative melting transition of DNA−Au NP aggregates at various ionic strengths is correlated to the particle size and DNA packing at the surface.[25,26] A number of components can also be incorporated into the DNA to tailor properties, such as photoswitchable azobenzenes that can tailor NP aggregation and sensing properties.[24] Moreover, it has also been discovered recently that DNA-guided crystallization of NPs can be achieved through careful control over these parameters and interactions.[16−19,24,30,31] This has led to a wealth of assembly phases,[23,24,31,32] stoichiometries, and symmetries.[16−19,30,33] Of particular importance is the potential for these interparticle linkages to be dynamic and reconfigurable.[33,34] This has been shown recently for the assembled crystals, as well as for NPs

* Address correspondence to mmmaye@syr.edu.

Received for review May 2, 2013 and accepted July 30, 2013.

Published online July 30, 2013
10.1021/nn402214e

assembled onto DNA scaffolds[35,36] and Origami patterns.[37,38]

Such reconfiguration may lead to smart solids and metamaterials, which react to environmental stimuli, much the same way that smart polymers react in bulk.[39−42] Recently, NPs have been modified with smart polymers for the first time.[43,44] Unlike the sequence-specific hybridization of DNA-modified NPs, smart polymer based assemblies have a stimuli-induced response, which takes advantage of the conformational changes in response to pH, light, or temperature changes.[45−47] For instance, temperature-responsive copolymers place emphasis on the monomer *N*-isopropylacrylamide (NIPAAm), which shows unique conformational behavior as a function of temperature.[39] Polymers of NIPAAm have a low critical solution temperature (LCST) of 32 °C, below which its chains are hydrated and form an expanded structure, and above which the chain undergoes collapse due to a combination of dehydration and depletion effects.[48,49] Such conformational changes are reversible, and important parameters such as the number of grafting points, grafting density, solvent conditions, and chain height[48,50−53] can affect the kinetics of temperature-responsive behavior of grafted polymers in comparison to bulk ones.[44,54] Researchers recently probed the temperature-responsive behavior of bulk and surface-grafted PNIPAAm and found that surface-bound polymers exhibited more gradual responses over a wider range of temperatures.[44,50,54] In addition, researchers have shown through careful parameter control that these polymers can be useful in a variety of applications such as drug delivery[55,56] and nanotechnology[43,57] and as a way to trigger cellular uptake.[58]

One potentially lucrative combination of DNA-encoded NPs and thermosensitive copolymers is for drug delivery. The DNA-capped NPs are effective for delivery of genes,[59,60] as well as for anticancer drugs such as doxorubicin[61,62] and platinum(IV) prodrugs.[63] Optimization of these designs also involves modifications with biomolecules such as serum proteins for enhanced cellular uptake[64] or aptamers for targeted delivery.[65] The co-modification of DNA-capped NPs with a temperature-sensitive smart polymer has not yet been performed to our knowledge, but the use of a LCST polymer that acts as a novel thermal switch that releases drug cargo from inside hollow gold nanocages has been shown and acts as inspiration.[55]

Herein, we describe how to modify the interface of Au NPs with both a thiol-modified temperature-responsive copolymer (pNIPAAm-*co*-pAAm) and thiol-modified single-stranded oligonucleotides (ssDNA). We show that conformational changes of the polymer can be used to regulate DNA recognition, which is blocked at low temperature due to the steric interference of the polymer, but promoted at high temperature due to the compression of the polymer shell below the hydrodynamic reach of the ssDNA. We further show that this steric effect influences the intercalation-based binding and release of the chemodrug doxorubicin at the DNA shell of an encoded nanocarrier, which results in a 6-fold increase in toxicity of the nanocarrier compared to previous studies.[61,62]

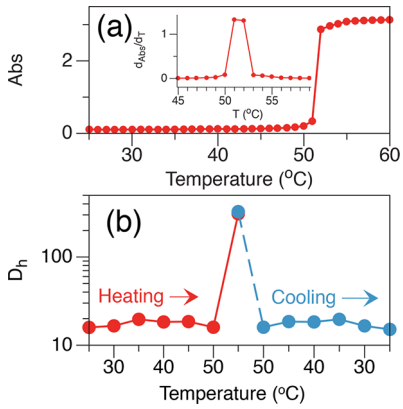

Figure 1. Thermal UV−vis showing the characteristic gel transition temperature for the copolymer (a). Representative DLS demonstrating the reversible temperature-induced conformational change of polymer chains in solution (b).

RESULTS AND DISCUSSION

A smart LCST pNIPAAm-*co*-pAAm copolymer (*p*) equipped with an internal disulfide linker was first synthesized following recently published work.[55] The monomer units' (NIPAAm, AAm) ratios could be tailored to modify the so-called critical temperature (T_C). In this system, a [NIPAAm]:[AAm] = 90:10 was used, and analysis by gel permeation chromatography (GPC) resulted in an average molecular weight of ∼290 000 g/mol (PDI = 1.12). Ultraviolet−visible absorption spectroscopy (UV−vis) was first used to determine the T_C of the polymer. UV−vis monitors the change in turbidity of the solution, which is the characteristic of the copolymers' aggregation as it changes from a hydrophilic state to the hydrophobic one.[55,56] Figure 1a shows a typical UV−vis result and reveals a sharp gel transition at T_C = 51 °C. This aggregation was further observed by dynamic light scattering (DLS), as shown in Figure 1b, which shows the reversible increase in hydrodynamic diameter (D_h) from D_h = 16 in monomer form to ∼330 nm in the aggregate/gel form at 51 °C. Further analysis by ^{1}H NMR (Figures S1, S2) and Fourier transform infrared spectroscopy (FTIR) (Figure S4) confirmed the structure. We next used the disulfide moiety of *p* to graft it to the Au NP interface.

The general strategy employed for NP functionalization and self-assembly is illustrated in Scheme 1a. To initiate binding of *p* to Au NP with a diameter (*D*) of 11.5 ± 1.1 nm (Figure S3), the disulfide linkage was first reduced to a thiol by reacting with tris(2-carboxyethyl)phosphine hydrochloride (TCEP)

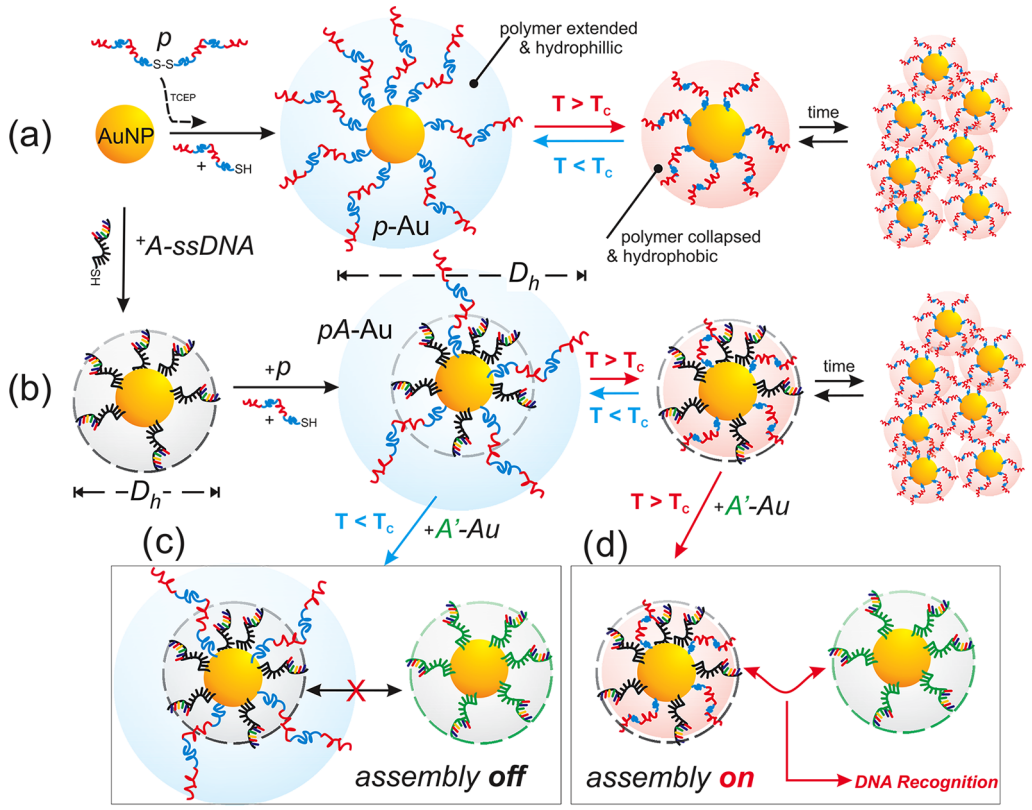

Scheme 1. Idealized schematic of the Au NP functionalization steps and assembly systems used in this study. (a) The Au NPs were functionalized with freshly reduced pNIPAAm-*co*-pAAm copolymer (*p*), and the thermal response based aggregation was measured. (b) The Au NPs were first functionalized with thiolated *A*-type ssDNA, then co-functionalized with *p*. The assembly of *Ap*-Au with complementary *A*′-Au was then blocked at $T < T_C$ (c), but promoted at $T > T_C$ (d).

at a 150× ratio for 30 min at room temperature, resulting in two *p*-chains (Figure S2). Then the *p* was added to 1 mL of Au NPs in a 12.5 molar excess ([*p*]:[Au] = 12.5) and left to anneal overnight. The excess *p* was removed by centrifugation at least three times for 1 h. The *p*-modified Au NPs (*p*-Au) were characterized by FTIR, thermal gravimetric analysis (TGA), and DLS. The FTIR of the *p*-Au showed the characteristic vibration signature of the *p*, which consisted of NIPAAm, AAm, and the disulfide linkage (Figure S4). TGA on the other hand characterized the mass loss of the *p*-Au, which is attributed to the loss of the *p*-capping. The average mass loss was ∼21%, a value that suggests that each *p*-Au has approximately 10 ± 2 chains per Au NP (Figure S5a). The *p*-modification was also observed by DLS (Figure 2), which showed a D_h increase from ∼12 to ∼58 nm for the citrate-capped Au NP precursors (i) and *p*-Au (ii), respectively.

To integrate the *p* into a DNA-capped Au NP system, we incubated both the thiol-laden *p* and ssDNA with the Au NPs, as shown in Scheme 1b (see Methods). We denote the DNA sequences used as *A*-type and complementary *A*′-type, and the ssDNA sequences are shown in Table 1. Each ssDNA consisted of a 15b encoded recognition end and a 15b poly-T spacer. The complementary ssDNA-capped (*A*′-Au) particles used to test DNA-based assembly were prepared analogously,

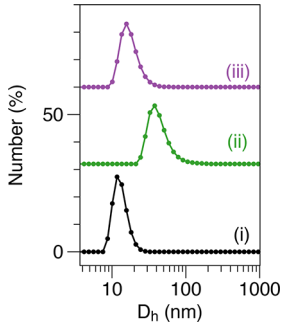

Figure 2. Representative DLS results for citrate-capped Au NPs (i), *p*-Au (ii), and *A*′-Au (iii) ([Au] = 1.2 nM, 0.2 M NaCl, 10 mM PB, pH = 7.4).

TABLE 1. ssDNA Used in This Study[a]

ssDNA	sequence (5′ to 3′)
A	TAC TTC CAA TCC AAT $(T)_{15}$-OC_3H_6-SH
A′	ATT GGA TTG GAA GTA $(T)_{15}$-OC_3H_6-SH
C	HS-C_6H_{12}O-(T)15 TGT TCG TAT TCG TAT TCG TC
C′	GAC GAA TAC GAA TAC GAA C

[a] Underlined sequences show high-affinity regions for doxorubicin (DOX) in *CC*′.

in the absence of *p*. The loading of *A* at the Au NP interface was quantified by using a fluorophore-tagged complementary strand (see supporting tables).[25,26,62] This quantification led to the average number of

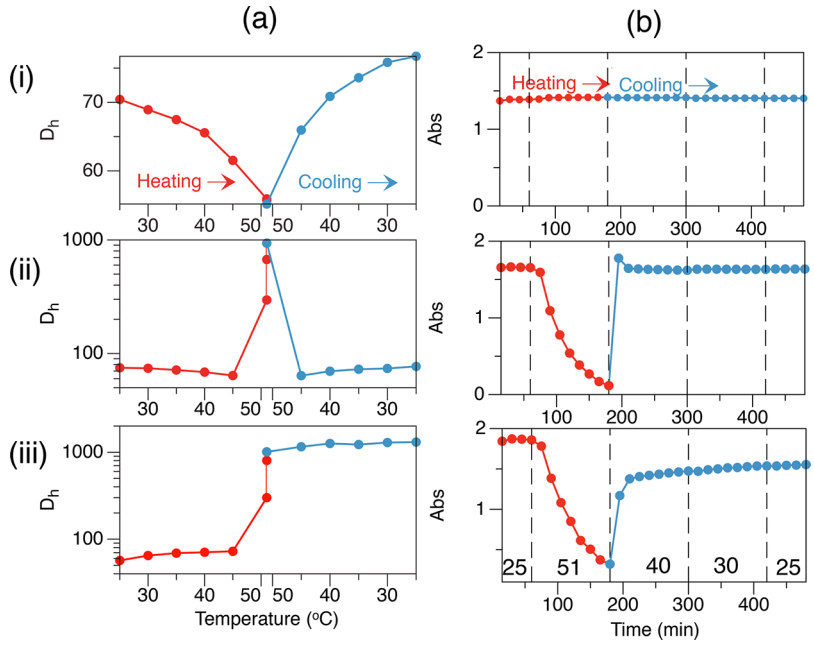

Figure 3. Representative DLS (a) and UV−vis (b) monitoring of thermal properties for *p*-Au (i), *Ap*-Au (ii), and *Ap*-Au + *A*′-Au (ii) measured from 25 to 51 °C (heating) and 51−25 °C (cooling), at 5° increments after 5 min of annealing time ([Au] = 1.2 nM (DLS) and 17.0 nM (UV−vis), 0.2 M NaCl, 10 mM PB, pH = 7.4).

A strands on the DNA−polymer-functionalized particles (*Ap*-Au) to be 64.4 ± 4.3 and *A* strands on the *A*-Au to be 65.8 ± 5.6. This is an interesting finding, as it suggests that the presence of the polymer did not necessarily decrease *A* coverage, likely due to the fact that the limiting factor for *A* loading is electrostatic interactions,[26] and since *p* is neutral, it did not affect this dynamic. Further analysis by TGA resulted in an increase in mass loss from ∼10% for *A*-Au (Figure S5c) and ∼22% for *Ap*-Au (Figure S5b), again suggesting the copresence of both *A* and *p* at the interface.

Once functionalized, the thermal properties of the three assembly systems, namely, *p*-Au, *Ap*-Au, and DNA−polymer-capped particles with the complementary particle (*Ap*-Au + *A*′-Au), were first characterized by DLS. Figure 3a-i investigates the thermal response of the *p*-Au under dilute concentrations ([*p*-Au] = 1.2 nM). When heated from 25 to 51 °C, we observed that the *z*-averaged D_h decreases from ∼70 to ∼55 nm, and upon decreasing back to 25 °C, the D_h reverses with a slight hysteresis showing a larger initial state (∼77 nm). The original $D_h \approx 70$ nm suggests that the *p* is in a highly extended brushlike state, likely due to the confinement of the chains at the 11.5 nm Au NP. The subsequent decrease in D_h is indicative that the *p*-shell is shrinking or compressing at or near T_C. It is generally accepted for LCST polymers that the phase transition to a hydrophobic state at $T > T_C$ is accompanied by an aggregation of the chains.[43,44] A similar transition has been observed for the polymer poly(*N*-isopropylacrylamide) when grafted onto planar surfaces.[44,50] The main difference between this DLS observation and that for the isolated *p* in Figure 1b is that in the latter case the polymer was in a concentrated solution (∼2.05 mg/mL), which results in significant interchain aggregation, whereas in the present case the concentration is much lower and the *p* is confined to the interface.

Figure 3a-ii shows a similar study for the mixed *p* + *A* interface of *Ap*-Au. Interestingly, the *Ap*-Au shows evidence of improved aggregation at 51 °C compared to *p*-Au, evident by the increase in D_h to ∼950 nm. Like the previous *p*-Au, the *Ap*-Au process is highly reversible, as indicated by the complete decrease in $D_h \approx 80$ nm upon cooling. These results show two interesting characteristics. First, the relatively large D_h of the *Ap*-Au at low *T* suggests that the *p*-chains are extended from the Au interface (similarly to the *p*-Au), since the *A*′-Au NPs have consistent $D_h \approx 20$ nm (Figure 2-iii). Second, the addition of the *A* at the interface improves the thermal response, as indicated by the rapid aggregation to $D_h \approx 940$ at $T > T_C$. This suggests that the distribution of the *p* at the NP interface and lower density improve the phase transition. Control experiments with *A*-Au at similar temperatures showed high colloidal stability (*i.e.*, negligible D_h change).

The highly reversible nature of the *Ap*-Au system was then tested in the presence of an equimolar concentration of complementary *A*′-Au. The DLS results for the *Ap*-Au + *A*′-Au system are shown in Figure 3a-iii and show a consistent $D_h \approx 73$ nm, similar to that observed for the *Ap*-Au system (∼80 nm). The lack of D_h increase at $T < T_C$ suggests that the *p*-surface is sterically limiting recognition. As the *Ap*-Au + *A*′-Au system reaches 51 °C, the D_h rapidly increases to >1000 nm. But, unlike the previous systems, upon cooling, it continues to

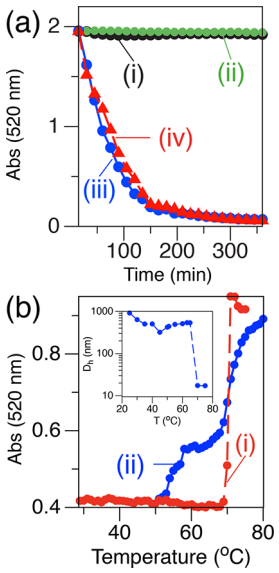

Figure 4. (a) UV−vis monitoring of assembly kinetics for *Ap*-Au + *A′*-Au at 25 °C (i), 40 °C (ii), and 51 °C (iii), in comparison with nonpolymer controls of *A*-Au + *A′*-Au at 51 °C (iv) ([Au] = 17 nM, 0.5 mM NaCl, 10 mM PB, pH = 7.4). (b) UV−vis monitring of thermal denaturation and disassembly for *A*-Au + *A′*-Au (i) and *Ap*-Au + *A′*-Au (ii). Inset: DLS monitoring of *Ap*-Au + *A′*-Au thermal denaturation and disassembly.

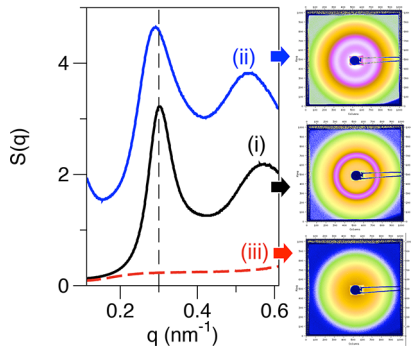

Figure 5. Synchrotron *in situ* SAXS results of the assembled aggregates from *A*-Au + *A′*-Au (i, q_1 = 0.303 nm^{-1}), *Ap*-Au + *A′*-Au (ii, q_1 = 0.290 nm^{-1}), and *Ap*-Au (iii, q_1 = 0.260 nm^{-1}) collected at λ = 1.1614 Å, 0.2 M PBS, and T = 25 °C.

increase, suggesting further aggregation and assembly. Since this system is irreversible, it suggests that the DNA linking is occurring, and this is only possible after the *p*-chains have been compressed at $T > T_C$. The consistent D_h at $T < T_C$, followed by the rapid increase in D_h at $T > T_C$, demonstrates thermal control over the sequence-specific hybridization between complementary particles, as well as further aggregation and assembly suggested by the continued increase in D_h upon cooling.

The temperature effects and assembly behavior were also characterized by UV−vis to monitor the change in absorbance. The absorbance of Au NP solutions is due to the surface plasmon resonance (SPR) of the Au NP, and its change in wavelength or extinction is indicative of change in local dielectric at the interface, self-assembly, and coupling of the SPR.[66] Figure 3b-i shows the SPR response of the *p*-Au during temperature increase from 25 °C to 51 °C. Little to no change is observed, suggesting no bulk aggregation occurs, in agreement with DLS. Figure 3b-ii demonstrates the behavior of the *Ap*-Au at 51 °C, which results in a decrease in absorbance, indicating NP aggregation, followed by an increase as the system cools. Figure 3b-iii shows the optical characteristics of the *Ap*-Au + *A′*-Au, which shows aggregation (absorbance decrease), followed by only a partial return, which is indicative of the stability of the small clusters or aggregates, *etc*. This incomplete recovery is the result of irreversible assembly, due to the formation of dsDNA linkages between Au, as suggested by DLS.

We further investigated the ability of the *p*-capping to regulate DNA-mediated assembly by monitoring assembly kinetics by UV−vis. For example, the kinetics of assembly for *Ap*-Au + *A′*-Au are shown in Figure 4a. At temperatures of 25 °C (i) and 40 °C (ii) there is no decrease in SPR (absorbance at 520 nm), which indicates little to no assembly, as described above. In contrast, at $T = T_C$ (iii), a rapid assembly occurs, as indicated by the drop in absorbance, due to the larger scattering cross section of the aggregate screening of NP extinction. The entire solution precipitated within 2 h. To better understand the driving force behind the assembly at $T = T_C$, the system was compared to a fully complementary *A*-Au + *A′*-Au control under the same conditions (iv). The kinetics were largely similar to the *Ap*-Au + *A′*-Au, indicating that at $T > T_C$ the *p*-chains have little influence.

To ensure that the assembly observed was indeed the result of DNA hybridization and not the temperature-induced response of the polymer, thermal denaturation studies were performed, as shown in Figure 4b. This DNA melting temperature (T_m) is higher than the *p*-transition, so discerning the two is possible. The complementary control, *A*-Au + *A′*-Au (i), shows a sharp melting transition at T_m = 69 °C, which is a characteristic of the cooperative behavior of the dsDNA chains at the interface.[61,62] By comparison, the *Ap*-Au + *A′*-Au system (ii) shows two transitions. The first is at T = 51−55 °C, and the second at T_m = 69 °C. The first transition is likely due to the affect of the *p* on the aggregate size, change of interparticle distances, or a combination thereof, whereas the second transition is the melting of the dsDNA linkages. In addition, the DNA transitions are rather broad, which is indicative of a decreased number of interparticle DNA linkages, which may suggest better separation of those linkages.[61] As discussed above, both the *Ap*-Au and *A*-Au have similar DNA densities (DNA/Au ≈ 65), which was why the T_m is similar, whereas the broadening is due to each linker being more electrostatically shielded due to the *p*-capping taking up space at the Au NP interface.[27]

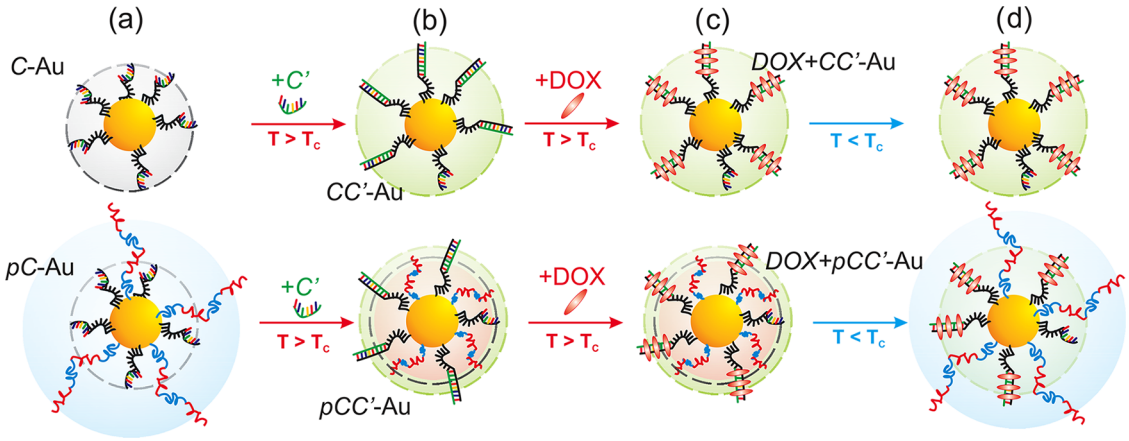

Scheme 2. Idealized schematic illustrating the preparation of the *CC′*-Au and *pCC′*-Au encoded nanocarriers from ssDNA (a) and dsDNA (b) moieties, to DOX loading (c), and the final nanocarrier before drug release at $T = 37$ and 53 °C.

The assembly behavior was further probed by investigating the interparticle spatial properties after assembly *via in situ* synchrotron small-angle X-ray scattering (SAXS). Figure 5 shows a representative set of SAXS scattering images and extracted structure factors ($S(q)$) for aggregates at 25 °C from the pure complementary control, *A*-Au + *A′*-Au (i), the complementary system plus polymer, *Ap*-Au + *A′*-Au (ii), and the colloidal solution of *Ap*-Au (iii). Each sample was assembled at 51 °C. The assembled aggregates showed two clear diffraction maxima, demonstrating reasonable ordering, whereas the *Ap*-Au showed only a small change to form factor, indicating no assembly occurs at room temperature. To better quantify these results, we approximated that the first diffraction, q_1, corresponds to the ⟨110⟩ plane of a body centered cubic (bcc) arrangement of Au NPs. We chose this model due to the similarity of this system to other two-strand binary systems that showed bcc crystallization and long-range order.[16−19,30] The lack of crystalline order in this system is most likely the result of the relatively short DNA linkages (*i.e.*, 15bp dsDNA + 30b ssDNA).[16−19]

Since $q_1 = 2\pi/d_{hkl}$, the lattice constant for the aggregates could be calculated from $1/d_{hkl} = (h^2 + k^2 + l^2)/a^2$, which allows for the nearest neighbor surface-to-surface distance (d^*) to be calculated *via* $d^* = (\sqrt{3}a/2) - D$, where D is the Au diameter (11.5 nm). This results in $d^* \approx 13.8$ and 15.0 nm for *A*-Au + *A′*-Au (i) and *Ap*-Au + *A′*-Au (ii), respectively. For the *A*-Au + *A′*-Au (i), this value is in agreement with a simple model for the interparticle distances of ∼13.5 nm, which considers the 15bp dsDNA linker and the two separate 15b poly-T spacers (Table 1, methods). Interestingly, these results show that the presence of the *p*-capping further extends this distance by ∼1.2 nm, likely due to steric effects between the polymer and the poly-T spacers. This is promoted by the fact that the aggregates assembled at 51 °C, which would have brought the *p*-capping and poly-T in close contact or forced the two to become intertwined. The effect of temperature on the interparticle distances was also studied; those results will be reported elsewhere.

Taken together, the irreversible assembly of the formed aggregates and the thermal denaturation of the *Ap*-Au + *A′*-Au assemblies at $T < T_C$ show that the *p*-chains block recognition, whereas at $T > T_C$ assembly occurs by DNA duplex formation. This ability to regulate assembly dynamics and interparticle spatial properties may be useful in regulating the bulk assembly and crystallization of the Au NPs, as has been shown recently.[16−20,31−33] This approach may also have utility in the use of the DNA-capped nanomaterials in drug and gene delivery, as described next.

We recently developed a novel approach to deliver chemotherapy drugs such as doxorubicin (DOX) and actinomycin D (ActD) to cancer cells. We call this system an encoded nanocarrier because it leverages the known dsDNA intercalating properties of drugs like DOX, which intercalate strongly at 5′-TCG sites.[61,62] In addition to dsDNA, intercalation has also been used with aptamer switches.[67] When the Au NP is capped with dsDNA, both DOX and ActD can be loaded at these high-affinity sequences, and the drugs can passively release over time with IC_{50} values comparable to the drug itself.[52] One limitation of our earlier approach however was the modest equilibrium constants for the DOX ($\sim 5 \times 10^6\ M^{-1}$),[62] which allows for diffusion away from the nanocarrier over times comparable to most toxicity studies.[68−71] To address this, we implemented the LCST polymer + DNA approach described above to create a next-generation system.

Scheme 2 shows the general drug loading strategy that implements the LCST behavior observed above. For example, Au NPs capped with dsDNA (*C*-type, *C′*-type) were prepared as described above (see Methods, Table 1).[61,62] In contrast to our previous studies, DOX loading of the *pCC′*-Au was performed at $T = 53$ °C in order to compress the *p* and promote complete drug loading. Drug loading was kept at [DOX]:[binding site] = 1 for all experiments. The concentrations of

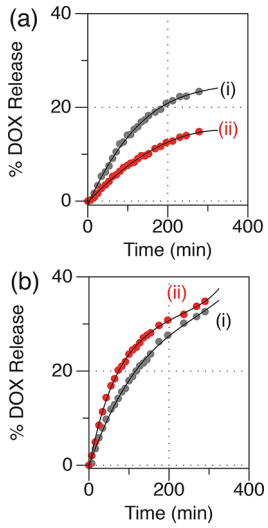

Figure 6. Results of dialysis experiments quantifying the percent DOX released from *CC′*-Au (i) and *pCC′*-Au (ii) at 37 °C (a) and at 53 °C (b). DOX was loaded at DOX:binding site = 1 ([Au] = 51, 61 nM, 0.2 M NaCl, 10 mM PB, pH = 7.4).

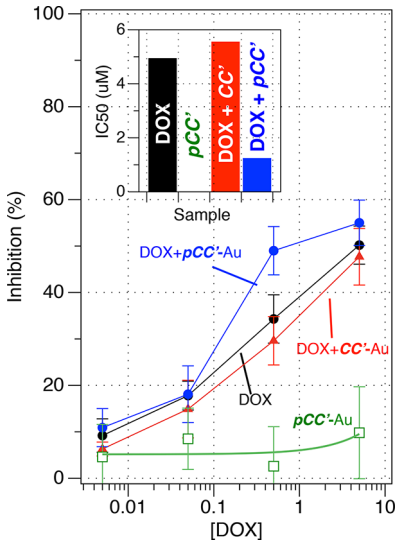

Figure 7. Percent inhibition of neuroblastoma SK-N-SH cells for DOX (black), DOX-*CC′*-Au (red), DOX-p*CC′*-Au (blue), and *pCC′*-Au (green). Inset: Calculated IC_{50} values.

TABLE 2. Kinetic and Equilibrium Results for the Release of DOX from *CC′*-Au and *pCC′*-Au at 37 and 53 °C

	37 °C		53 °C	
	DOX-*CC′*-Au	DOX-*pCC′*-Au	DOX-*CC′*-Au	DOX-*pCC′*-Au
α (%)[a]	28.8	21.5	39.1	35.0
β (min^{-1})[a]	6.35×10^{-3}	4.29×10^{-3}	6.16×10^{-3}	1.12×10^{-2}
K (M^{-1})[b]	9.4×10^{6}	1.9×10^{7}	4.4×10^{6}	5.9×10^{6}

[a] Results of fit to eqs 1 and 2. [b] Results of fit to eq 4.

CC′-Au and *pCC′*-Au relative to the DOX concentration were varied based on the number of binding sites per *CC′* duplex, which were 64.5 ± 2.5 and 53.9 ± 10.6 *CC′* duplexes/NP for the *CC′*-Au and *pCC′*-Au systems, respectively.

To quantify drug release, dialysis experiments were performed in which both the DOX-loaded DOX-*CC′*-Au and DOX-*pCC′*-Au were placed inside a dialysis membrane and either the fluorescence or absorbance of DOX was measured outside the membrane at 37 and 53 °C.[61] Figure 6 shows the kinetics for drug release at 37 °C (a) for the DOX-*CC′*-Au (i) compared to the equivalent DOX-*pCC′*-Au (ii). Interestingly, these results show that the polymer environment at the Au interface successfully slows drug release. Table 2 tabulates the DOX release percent, as well as drug release rate constant and final equilibrium values. Of particular importance is the near 50% increase in equilibrium (eq 4, Supporting Information), demonstrating that less drug is released per unit time. Interestingly, at 53 °C ($T > T_C$), these trends are reversed, and the DOX-*pCC′*-Au system shows faster DOX release compared to DOX-*CC′*-Au (Figure 6b). These results show that the dynamic and thermoresponsive properties of the incorporated *p*-chains have a dramatic effect on local DNA environment. We note that photothermal systems have also been be employed for drug release in studies involving micelles and liposomes with transition temperatures of ~40 °C,[67,72] as well as model drug release from gold nanorods.[73]

Cytotoxicity studies were then performed to evaluate the inhibition of neuroblastoma (SK-N-SH) cancer cell growth by DOX, DOX-*CC′*-Au, and DOX-p*CC′*-Au. Figure 7 shows that the percent inhibition is enhanced for the DOX-*pCC′*-Au relative to both DOX and DOX-*CC′*-Au, particularly at 0.5 and 5 μM DOX. At these concentrations, inhibition by DOX-*pCC′*-Au significantly exceeds the inhibition by the DOX control. This effect seems to result from the greatly improved equilibrium constant for *pCC′*-Au, which permits more DOX molecules to remain attached to the nanocarrier during exposure to cells. Of particular importance, the estimated IC_{50} value of the *pCC′*-Au is decreased 4-fold relative to DOX and ~4.5-fold relative to *CC′*-Au, thus demonstrating this next-generation system is highly viable (Figure 7, Table S2). Moreover, the *pCC′*-Au controls showed little toxicity to the cells.

Taken together, these results show that it is possible to use the reconfigurable conformation of thermosensitive copolymers to tailor both DNA-mediated assembly of nanoparticles and drug delivery. In the current design, the thermal response is below the DNA melting temperatures; however future studies may have T_C values either comparable to or greater than T_m. This may allow for a number of new properties, such as the locking of assemblies, improved thermal stability, or the introduction of new mechanisms for dynamic reconfiguration.[34] This may have particular importance in the 3D crystallization of the assemblies, where steric interactions, coordination, and interparticle energy landscapes are critical.[15,30] In addition, by varying the

chain length of the ssDNA utilized,[16−19] either by increasing its rigidity[28] or by adding linker strands,[32,32] the effects of the polymer can be further fine-tuned and understood. The dynamic presence of the polymer can also be further tuned for drug delivery and bioimaging *in vivo* if the T_C is tuned to be closer to body temperature. Furthermore, the polymer may be used a further docking site for cell targeting molecules, such as peptides and small molecules. Such studies in both self-assembly and drug delivery are currently under way.

CONCLUSIONS

In summary, an LCST smart polymer consisting of pNIPAAm-*co*-pAAm copolymers equipped with a thiol termination was synthesized and grafted onto gold nanoparticle interfaces that were cofunctionalized with single-stranded oligonucleotides. At $T < T_C$, the chains extend beyond the hydrodynamic reach of the ssDNA and prohibit recognition. However, at $T > T_C$, assembly was observed, due in large part to the hydrophobic collapse of the polymer chains and the subsequent exposure of the complementary DNA bases. Also observed was the reversible thermal flocculation of the DNA + polymer NPs themselves under concentrated conditions, an effect attributed to depletion at the NP interface. SAXS confirmed aggregate ordering and the role that the polymer plays in extending interparticle distances. Finally, the potential applicability of this system was explored by incorporating its design into an encoded nanocarrier drug delivery system. It was found that the presence of the polymer increases equilibrium at $T < T_C$, but decreases it at $T > T_C$, thus allowing for the successful improvement of the drug delivery design. Cytotoxicity studies confirmed this design improvement, demonstrating that the polymer + encoded nanocarrier produces a 4-fold improvement in IC_{50} relative to the established chemotherapeutic agent doxorubicin.

METHODS

Nanoparticle Synthesis. Gold nanoparticles (Au) with a diameter (D) of 11.5 ± 1.1 nm were synthesized by a citrate reduction procedure.[28] The Au concentrations were calculated using Beers law with an extinction coefficient (ε) of 1.0×10^8 L mol^{-1} cm^{-1}.

Polymer Synthesis. The LCST copolymer (p) was prepared using *N*-isopropylacrylamide and acrylamide subunits. The pNIPAAm-*co*-pAAm polymer (p) was prepared *via* an atom transfer radical polymerization.[55] A NIPAAm:AAm monomer ratio of 90:10 was used to achieve a critical temperature (T_C) of 51 °C. In a typical synthesis, the monomers were dissolved in ultrapure water and methanol and allowed to react at room temperature for 20 min, after which the disulfide-containing initiator bis[2-(2′-bromoisobutyryloxy)ethyl] disulfide [$(BiBOE)_2S_2$] was added along with *N*,*N*,*N*′,*N*′,*N*″-pentamethyldiethylenetriamine. The sample was stirred at room temperature for 20 min, then frozen and degassed under vacuum. To the frozen sample was added an excess of CuBr; then the sample was thawed at room temperature, purged under argon, and allowed to stir overnight. After reacting overnight the resulting blue gel was dispersed in ultrapure water (10 mL) and purified by dialysis. After purification, GPC analysis revealed a molecular weight of 290 000 (PDI = 1.12), and ^{1}H NMR (Figures S1 and S2) confirmed the composition. The thermal properties were analyzed by UV−vis and DLS.

Polymer Functionalization. To initiate binding of the p to the Au surface (p-Au), the disulfide linkage of p was first reduced with a 150× ratio of tris(2-carboxyethyl)phosphine hydrochloride for 30 min at room temperature. Then the p was added to 1 mL of Au NPs in a 12.5 molar excess ([p]:[Au] = 12.5) and left to anneal overnight. Excess p was removed by complete centrifugation of p-Au at least three times, and the final product was stable in ultrapure water, as well as buffers with ionic strengths up to 200 mM. In addition, trace amounts of TCEP may also reside on the Au. Control experiments purposely using TCEP-modified Au showed no self-assembly or temperature-dependent properties.

DNA and DNA + Polymer Functionalization. The DNA-capped Au were prepared by the standard Mirkin method.[26] The thiol-modified oligonucleotides (see Table 1) were first reduced from disulfides using 100 mM dithiothreitol and purified by an Illustra NAP-25 column (GE Healthcare, UK Ltd.), eluted with 10 mM phosphate buffer (pH = 7.2). The DNA was quantified using the sequence-specific extinction coefficient. Next, the reduced DNA was added to a 1 mL aliquot of the Au NP in a 250 molar excess ([DNA]:[Au NP] = 250), left to anneal at room temperature overnight, and then slowly salt aged using NaCl to a final ionic strength of 200 mM.[26] The excess DNA was removed by complete centrifugation of the DNA-Au at least three times. To cofunctionalize the surface of the Au NPs with both p and DNA, aspects of both individual functionalization procedures were used. First, the reduced DNA (*i.e.*, *A*-type) was added at similar ratios to that described above and left to anneal in 10 mM phosphate buffer (pH = 7.2). The ionic strength was then gradually increased to 50 mM and left to anneal overnight. Next, the p was added for 12 h at ratios described above, followed by salt aging. The p was added at this early salt-aging step to ensure there was sufficient empty space to accommodate multiple p-chains. These optimized conditions were based on additional experiments (not shown) that demonstrated the necessity of introducing some ionic strength stability to the Au (by adding DNA first) to ensure effective cofunctionalization. For instance, having full coverage of DNA on Au before addition of p limited p-loading and *vice versa*. Those results will be described in detail elsewhere. The number of active duplexes per Au NP at 25 °C was determined by fluorescence tags to be 56.3 ± 1.1 for the *AA*′-Au and 46.7 ± 1.3 for the *pAA*′-Au (Table S1).

Encoded Nanocarrier. The DNA-capped Au with *C*-capping and *pC*-capping was prepared analogously to that described above.[28] After purification, the *pC*-Au was hybridized with *C*′ as previously reported,[61,62] to produce *pCC*′-Au. Both *CC*′-Au and *pCC*′-Au were incubated with DOX for 40 min prior to dialysis experiments. DOX loading for the *pCC*′-Au system was performed at 53 °C to promote complete drug loading in the presence of the polymer. In order to keep DOX/binding site = 1 for all experiments, the concentrations of *CC*′-Au and *pCC*′-Au relative to the DOX concentration were varied based on the number of binding sites per *CC*′ duplex, in which each *CC*′ duplex had three high-affinity sequences (Supporting Information). The number of active *CC*′ duplexes per Au NP was determined by fluorescence tags to be 64.5 ± 2.5 for the *CC*′-Au and 53.9 ± 10.6 for the *pCC*′-Au.

Conflict of Interest: The authors declare no competing financial interest.

Supporting Information Available: Supporting Figures S1−S5, calculations, and additional experimental details. This material is available free of charge *via* the Internet at http://pubs.acs.org.

Acknowledgment. This work was supported by the Air Force Office of Scientific Research (AFOSR, FA9550-10-1-0033).

Additional student support provided by the National Science Foundation (NSF-IGERT, DGE-1068780, NSF-iREU, 02190—CON01914, NSF-REU, 1156942), the Syracuse Biomaterials Institute (SBI), and the Syracuse University Forensics and National Security Science Institute (FNSSI) is acknowledged. We thank Deb Kerwood at the SU NMR facility for NMR assistance, Prof. Rebekka Bader and Prof. Patrick Mather at the Syracuse Biomaterials Institue (SBI) for assistance with GPC analysis, and Robert Smith at SUNY-ESF for TEM assistance. D.R. acknowledges an NSF-iREU fellowship (Chemistry), and C.P. acknowledges an NSF-REU fellowship (SBI). The Cornell High Energy Synchrotron Source (CHESS) is supported by the NSF (DMR-0936384) and the NIH/NIGMS (GM-103485). We thank Dr. Detlef Smilgies at CHESS for SAXS assistance.

REFERENCES AND NOTES

1. Katz, E.; Willner, I. Integrated Nanoparticle-Biomolecule Hybrid Systems: Synthesis, Propterties, and Applications. *Angew. Chem.* **2004**, *43*, 6042–6108.
2. Yeh, Y.-C.; Creran, B.; Rotello, V. M. Gold Nanoparticles: Preparation, Properties, and Applications in Bionanotechnology. *Nanoscale* **2012**, *4*, 1871–1880.
3. Zhang, Z.; Horsch, M. A.; Lamm, M. H.; Glotzer, S. C. Tethered Nano Building Blocks: Towards a Conceptual Framework for Nanoparticle Self-Assembly. *Nano Lett.* **2003**, *3*, 1341–1346.
4. Daniel, M. C.; Astruc, D. Gold Nanoparticles: Assembly, Supermolecular Chemistry, Quantum-Size-Related Properties, and Applications toward Biology, Catalysis, and Nanotechnology. *Chem. Rev.* **2004**, *104*, 293–346.
5. Zamborini, F. P.; Hicks, J. F.; Murray, R. W. Quantized Double Layer Charging of Nanoparticle Films Assembled Using Carboxylate/(Cu^{2+} or Zn^{2+})/Carboxylate Bridges. *J. Am. Chem. Soc.* **2000**, *122*, 4514–4515.
6. Zheng, W.; Maye, M. M.; Leibowitz, F. L.; Zhong, C. J. Imparting Biomimetic Ion-Grating Recognition to Electrodes with a Hydrogen-Bonding Structured Core-Shell Nanoparticle Network. *Anal. Chem.* **2000**, *72*, 2190–2199.
7. Templeton, A. C.; Wuelfing, W. P.; Murray, R. W. Monolayer-Protected Cluster Molecules. *Acc. Chem. Res.* **2000**, *33*, 27–36.
8. Fresco, Z. M.; Fréchet, J. M. Selective Surface Activation of a Functional Monolayer for the Fabrication of Nanometer Scale Thiol Patterns and Directed Self-Assembly of Gold Nanoparticles. *J. Am. Chem. Soc.* **2005**, *127*, 8302–8303.
9. Maye, M. M.; Chun, S. C.; Han, L.; Rabinovich, D.; Zhong, C. J. Novel Spherical Assembly of Gold Nanoparticles Mediated by a Tetradentate Thioether. *J. Am. Chem. Soc.* **2002**, *124*, 4958–4959.
10. Maye, M. M.; Lim, I. I. S.; Luo, J.; Rab, Z.; Rabinovich, D.; Liu, T.; Zhong, C. J. Mediator-Template Assembly of Nanoparticles. *J. Am. Chem. Soc.* **2005**, *127*, 1519–1529.
11. Frankamp, B. L.; Boal, A. K.; Rotello, V. M. Controlled Interparticle Spacing through Self-Assembly of Au Nanoparticles and Poly(amidoamine) Dendrimers. *J. Am. Chem. Soc.* **2002**, *124*, 15146–15147.
12. Boal, A. K.; Rotello, V. M. Fabrication and Self-Optimization of Multivalent Receptors on Nanoparticle Scaffolds. *J. Am. Chem. Soc.* **2000**, *122*, 734–735.
13. Boal, A. K.; Ilhan, F.; DeRouchey, J. E.; Thurn-Albrecht, T.; Russell, T. P.; Rotello, V. M. Self-Assembly of Nanoparticles into Structured Spherical and Network Aggregates. *Nature* **2000**, *404*, 746–748.
14. Ofir, Y.; Samanta, B.; Rotello, V. M. Polymer and Biopolymer Mediated Self-Assembly of Gold Nanoparticles. *Chem. Soc. Rev.* **2008**, *37*, 1814–1825.
15. Maye, M. M.; Nykypanchuk, D.; van der Lelie, D.; Gang, O. DNA-Regulated Micro- and Nanoparticle Assembly. *Small* **2007**, *3*, 1678–1692.
16. Nykypanchuck, D.; Maye, M. M.; van der Lelie, D.; Gang, O. DNA Guided Crystalline Organization of Nanoparticles. *Nature* **2008**, *451*, 549–552.
17. Xiong, H.; van der Lelie, D.; Gang, O. Phase Behavior of Nanoparticles Assembled by DNA Linkers. *Phys. Rev. Lett.* **2009**, *102*, 015504.
18. Xiong, H.; van der Lelie, D.; Gang, O. DNA Linker-Mediated Crystallization of Nanoparticles. *J. Am. Chem. Soc.* **2008**, *130*, 2442–2443.
19. Sun, D.; Gang, O. Binary Heterogeneous Superlattices Assembled from Quantum Dots and Gold Nanoparticles with DNA. *J. Am. Chem. Soc.* **2011**, *133*, 5252–5254.
20. Park, S. Y.; Lytton-Jean, A. K. R.; Lee, B.; Weigand, S.; Schatz, G. C.; Mirkin, C. A. DNA-Programmable Nanoparticle Crystallization. *Nature* **2008**, *451*, 553–556.
21. Alivisatos, A. P.; Johnsson, K. P.; Peng, X.; Wilson, T. E.; Loweth, C. J.; Bruchez, M. P.; Schultz, P. G. Organization of 'Nanocrystal Molecules' Using DNA. *Nature* **1996**, *382*, 609–611.
22. Mann, S.; Shenton, W.; Li, M.; Connolly, S.; Fitzmaurice, D. Biologically Programed Nanoparticle Assembly. *Adv. Mater.* **2000**, *12*, 147–150.
23. Jones, M. R.; Macfarlane, R. J.; Lee, B.; Zhang, J.; Young, K. L.; Senesi, A. J.; Mirkin, C. A. DNA-Nanoparticle Superlattices Formed from Anisotropic Building Blocks. *Nat. Mater.* **2010**, *9*, 913–917.
24. Yan, Y. Q.; Chen, J. I. L.; Ginger, D. S. Photoswitchable Oligonucleotide-Modified Gold Nanoparticles: Controlling Hybridization Stringency with Photon Dose. *Nano Lett.* **2012**, *12*, 2530–2536.
25. Hurst, S. J.; Hill, H. D.; Mirkin, C. A. Three-Dimensional Hybridization with Polyvalent DNA-Gold Nanoparticle Conjugates. *J. Am. Chem. Soc.* **2008**, *130*, 12192–12200.
26. Hurst, S. J.; Lytton-Jean, A. K. R.; Mirkin, C. A. Maximizing DNA Loading on a Range of Gold Nanoparticle Sizes. *Anal. Chem.* **2006**, *78*, 8313–8318.
27. Jin, R.; Wu, G.; Li, Z.; Mirkin, C. A.; Schatz, G. C. What Controls the Melting Properties of DNA-Linked Gold Nanoparticle Assemblies? *J. Am. Chem. Soc.* **2003**, *125*, 1643–1654.
28. Maye, M. M.; Nykypanchuk, D.; van der Lelie, D.; Gang, O. A Simple Method for Kinetic Control of DNA-Induced Nanoparticle Assembly. *J. Am. Chem. Soc.* **2006**, *128*, 14020–14021.
29. Baker, B. A.; Milam, V. T. DNA Density-Dependent Assembly Behavior of Colloidal Micelles. *Langumir* **2010**, *26*, 9818–9826.
30. Maye, M. M.; Kumara, M. T.; Nykypanchuk, D.; Sherman, W. B.; Gang, O. Switching Binary States of Nanoparticle Superlattices and Dimer Clusters by DNA Strands. *Nat. Nanotechnol.* **2010**, *5*, 116–120.
31. Hill, H. D.; Macfarlane, R. J.; Senesi, A. J.; Lee, B.; Park, S. Y.; Mirkin, C. A. Controlling the Lattice Parameters of Gold Nanoparticle FCC Crystals with Duplex DNA Linkers. *Nano Lett.* **2008**, *8*, 2341–2344.
32. Auyeung, E.; Culter, J. L.; Macfarlane, R. J.; Jones, M. R.; Wu, J.; Liu, J.; Zhang, K.; Osberg, K. D.; Mirkin, C. A. Synthetically Programmable Nanoparticle Superlattices Using a Hollow Three Dimensional Spacer Approach. *Nat. Lett.* **2012**, *7*, 24–28.
33. Maye, M. M.; Nykypanchuk, D.; Cuisinier, M.; Lelie, D. V. D.; Gang, O. Stepwise Surface Encoding for High-Thoroughput Assembly of Nanoclusters. *Nat. Mater.* **2009**, *8*, 388–391.
34. Valignat, M. P.; Theodoly, O.; Crocker, J. C.; Russel, W. B.; Chaikin, P. M. Reversible Self-Assembly and Directed Assembly of DNA-Linked Micrometer-Sized Colloids. *Proc. Natl. Acad. Sci. U.S.A.* **2005**, *102*, 4225–4229.
35. Claridge, S. A.; Goh, S. L.; Fréchet, J. M. J.; Williams, S. C.; Micheel, C. M.; Alivisatos, A. P. Directed Assembly of Discrete Gold Nanoparticle Groupings Using Branched DNA Scaffolds. *Chem. Mater.* **2005**, *17*, 1628–1635.
36. Liu, D.; Wang, M.; Deng, Z.; Walulu, R.; Mao, C. Tensegrity: Construction of Rigid DNA Triangles with Flexible Four-Arm DNA Junctions. *J. Am. Chem. Soc.* **2004**, *126*, 2324–2325.
37. Rothemund, P. W. K. Folding DNA to Create Nanoscale Shapes and Patterns. *Nature* **2006**, *440*, 297–302.
38. Tørring, T.; Voigt, N. V.; Nangreave, J.; Yan, H.; Gothelf, K. V. DNA Origami: A Quantum Leap for Self-Assembly of Complex Structures. *Chem. Soc. Rev.* **2011**, *40*, 5636–5646.
39. Zhang, J.; Pelton, R.; Deng, Y. Temperature-Dependent Contact Angles of Water on Poly(N-Isopropylacrylamide) Gels. *Langmuir* **1995**, *11*, 2301–2302.

40. Wei, H.; Cheng, S. X.; Zhang, X. Z.; Zhuo, R. X. Thermo-Sensitive Micelles Based on Poly(N-Isopropylacrylamide) as Drug Carriers. *Prog. Polym. Sci.* **2009**, *34*, 893–910.
41. Heredia, K. L.; Bontempo, D.; Ly, T.; Byers, J. T.; Hastenberg, S.; Maynard, H. D. *In Situ* Preparation of Protein-"Smart" Polymer Conjugates with Retention of Bioactivity. *J. Am. Chem. Soc.* **2005**, *127*, 16955–16960.
42. Bergreiter, D. E.; Case, B. L.; Liu, Y. S.; Caraway, J. W. Poly-(N-Isopropylacrylamide) Soluble Polymer Supports in Catalysis and Synthesis. *Macromolecules* **1998**, *31*, 6053–6062.
43. Zhu, M. Q.; Wang, L. Q.; Exarhos, G. J.; Li, A. D. Q. Thermosensitive Gold Nanoparticles. *J. Am. Chem. Soc.* **2004**, *126*, 2656–2657.
44. Chakraborty, S.; Bishnoi, S. W.; Perez-Luna, V. H. Gold Nanoparticles with Poly(N-Isopropylacrylamide) Formed *via* Surface Initiated Atom Transfer Free Radical Polymerization Exhibit Unusually Slow Aggregation Kinetics. *J. Phys. Chem. C* **2010**, *114*, 5947–5955.
45. Grunlan, J. C.; Liu, L.; Kim, Y. S. Tunable Single-Walled Carbon Nanotube Microstructure in the Liquid and Solid States Using Poly(acrylic acid). *Nano Lett* **2006**, *6*, 911–915.
46. Jochum, F. D.; Theato, P. Thermo- and Light Responsive Micellation of Azobenzene Containing Block Copolymers. *Chem. Commun.* **2010**, *46*, 6717–6719.
47. Lee, R. S.; Huang, Y. T.; Chen, W. H. Synthesis and Characterization of Temperature-Sensitive Block Copolymers from Poly(N-Isopropylacrylamide) and 4-Methyl-ε-caprolactone or 4-Phenyl-ε-caprolactone. *J. Appl. Polym. Sci.* **2010**, *118*, 1634–1642.
48. Takei, Y. G.; Aoki, T.; Sanui, K.; Ogata, N.; Sakurai, Y.; Okano, T. Dynamic Contact Angle Measurement of Temperature-Responsive Surface Properties for Poly(N-Isopropylacrylamide) Grafted Surfaces. *Macromolecules* **1994**, *27*, 6163–6166.
49. Gong, X.; Wu, C.; Ngai, T. Surface Interaction Forces Mediated by Poly(N-Isopropylacrylamide) (PNIPAM) Polymers: Effects of Concentration and Temperature. *Colloid Polym. Sci.* **2010**, *288*, 1167–1172.
50. Balamurugan, S.; Mendez, S.; Balamurugan, S. S.; O'Brian, M. J.; López, G. P. Thermal Response of Poly(N-Isopropylacrylamide) Brushes Probed by Surface Plasmon Resonance. *Langmuir* **2003**, *19*, 2545–2549.
51. Yim, H.; Kent, M. S. Temperature-Dependent Conformational Change of PNIPAM Grafted Chains at High Surface Density in Water. *Macromolecules* **2004**, *37*, 1994–1997.
52. Yim, H.; Kent, M. S.; Huber, D. L. Conformation of End-Tethered PNIPAM Chains in Water and in Acetone by Neutron Reflectivity. *Macromolecules* **2003**, *36*, 5244–5251.
53. Jones, D. M.; Smith, J. R.; Huck, W. T. S.; Alexander, C. Variable Adhesion of Micropatterned Thermoresponsive Polymer Brushes: AFM Investigations of Poly(N-Isopropylacrylamide) Brushes Prepared by Surface-Initiated Polymerizations. *Adv. Mater.* **2002**, *14*, 1130–1134.
54. Chirra, H. D.; Hilt, Z. J. Nanoscale Characterization of the Equilibrium and Kinetic Response of Hydrogel Structures. *Langmuir* **2010**, *26*, 11249–11257.
55. Yavuz, M. S.; Cheng, Y.; Chen, J.; Cobley, C. M.; Zhang, Q.; Rycenga, M.; Xie, J.; Kim, C.; Song, K. H.; Schwartz, A. G.; Wang, L. V.; Xia, Y. Gold Nanocages Covered by Smart Polymers for Controlled Release with Near-Infrared Light. *Nat. Mater.* **2009**, *8*, 935–939.
56. Wei, H.; Zhang, X.; Cheng, C.; Cheng, S. X.; Zhuo, R. X. Self-Assembled Thermosensitive Micelles of a Star Block Copolymer Based on PMMA and PNIPAAm for Controlled Drug Delivery. *Biomaterials* **2007**, *28*, 99–107.
57. Ito, T.; Hioki, T.; Yamaguchi, T.; Shinbo, T.; Nakao, S. I.; Kimura, S. Development of a Molecular Recognition Ion Grating Membrane and Estimation of Its Pore Size Control. *J. Am. Chem. Soc.* **2002**, *124*, 7840–7846.
58. Kim, C.; Lee, Y.; Kim, J. S.; Jeong, J. H.; Park, T. G. Thermally Triggered Cellular Uptake of Quantum Dots Immobilized with Poly(N-isopropylacrylamide) and Cell Penetrating Peptide. *Langmuir* **2010**, *26*, 14965–14969.
59. Rosi, N. L.; Giljohann, D. A.; Thaxton, C. S.; Lytton-Jean, A. K. R.; Han, M. S.; Mirkin, C. A. Oligonucleotide-Modified Gold Nanoparticles for Intracellular Gene Regulation. *Science* **2006**, *312*, 1027–1030.
60. Rosi, N. L.; Mirkin, C. A. Nanostructures in Biodiagnostics. *Chem. Rev.* **2005**, *105*, 1547–1562.
61. Alexander, C. M.; Maye, M. M.; Dabrowiak, J. C. DNA-Capped Nanoparticles Designed for Doxorubicin Drug Delivery. *Chem. Commun.* **2011**, *47*, 3418–3420.
62. Alexander, C. M.; Dabrowiak, J. C.; Maye, M. M. Investigation of the Drug Binding Properties and Cytotoxicity of DNA-Capped Nanoparticles Designed as Delivery Vehicles for the Anticancer Agents Doxorubicin and Actinomycin D. *Bioconjugate Chem.* **2012**, *23*, 2061–2070.
63. Dhar, S.; Daniel, W. L.; Giljohann, D. A.; Mirkin, C. A.; Lippard, S. J. Polyvalent Oligonucleotide Gold Nanoparticle Conjugates as Delivery Vehicles for Platinum (IV) Warheads. *J. Am. Chem. Soc.* **2009**, *131*, 14652–14653.
64. Patel, P. C.; Giljohann, D. A.; Daniel, W. L.; Zheng, D.; Prigodich, A. E.; Mirkin, C. A. Scavenger Receptors Mediate Cellular Uptake of Polyvalent Oligonucleotide-Functionalized Gold Nanoparticles. *Bioconjugate Chem.* **2010**, *21*, 2250–2256.
65. Kim, D.; Jeong, Y. Y.; Jon, S. A Drug-Loaded Aptamer-Gold Nanoparticle Bioconjugate for Combined CT Imaging and Therapy of Prostate Cancer. *ACS Nano* **2010**, *4*, 3689–3696.
66. Burda, C.; Chen, X.; Narayanan, R.; El-Sayed, M. A. Chemistry and Properties of Nanocrystals of Different Shapes. *Chem. Rev.* **2005**, *105*, 1025–1102.
67. Bagalkot, V.; Zhang, L.; Levy-Nissenbaum, E.; Jon, S.; Kantoff, P. W.; Langer, R.; Farokhzad, O. C. Quantum Dot-Aptamer Conjugates for Synchronous Cancer Imagining, Therapy, and Sensing of Drug Delivery Based on Bi-Fluorescence Resonance Energy Transfer. *Nano Lett.* **2007**, *7*, 3065–3070.
68. Wang, F.; Wang, Y.; Dou, S.; Xiong, M.; Sun, T.; Wang, J. Doxorubicin-Tethered Responsive Gold Nanoparticles Facilitate Intracellular Drug Delivery for Overcoming Multidrug Resistance in Cancer Cells. *ACS Nano* **2011**, *5*, 3679–3692.
69. Yoo, H. S.; Park, T. G. Folate-Receptor-Targeted Devlivery of Doxorubicin Nano-Aggregates Stabilized by Doxorubicin-PEG-Folate Conjugate. *J. Controlled Release* **2004**, *100*, 247–256.
70. Konsoula, R.; Barile, F. A. Correlation of *in Vitro* Cytotoxicity with Permeability in Mortal Rat Intestinal Cells. *J. Pharmacol. Toxicol. Methods* **2007**, *55*, 176–183.
71. Needham, D.; Anyarambhatla, G.; Kong, G.; Dewhirst, M. W. A New Temperature-Sensitive Liposome for Use with Mild Hyperthermia: Characterization and Testing in a Human Tumor Xenograft Model. *Cancer Res.* **2000**, *60*, 1197–1201.
72. Liu, S. Q.; Tong, Y. W.; Yang, Y. Y. Thermally Sensitive Micelles Self-Assembled from Poly(N-isopropylacrylamide-co-N,N-dimethylacrylamide)-b-poly(D,L-lactide-co-glycolide) for Controlled Delivery of Paclitaxel. *Mol. BioSyst.* **2005**, *1*, 158–165.
73. Huang, J.; Jackson, K. S.; Murphy, C. J. Polyelectrolyte Wrapping Layers Control Rates of Photothermal Molecular Release from Gold Nanorods. *Nano Lett.* **2012**, *12*, 2982–2978.